J. Fluid Mech. (2012), *vol.* 712, *pp.* 624–645.
doi:10.1017/jfm.2012.389

Sedimentation from binary suspensions in a turbulent gravity current along a V-shaped valley

Catherine A. Mériaux† and Cathy B. Kurz-Besson

Instituto Dom Luiz, Departamento de Engenharia Geografica, Geofisica e Energia, Faculdade de Ciências, Universidade de Lisboa, Campo Grande 1749-016 Lisboa, Portugal

(Received 6 December 2011; revised 19 June 2012; accepted 31 July 2012; first published online 13 September 2012)

We present a study of bidispersed particulate gravity currents at high Reynolds numbers flowing along a V-shaped valley. The speed and width of the currents, the mass deposited by the currents and the density of the deposits were examined by both a box model and lock-exchange experiments in a 5 m long tank. Silicon carbide and glass beads were used for the bidispersed suspension models. The initial conditions of the currents were similar, except that the grain size of the glass beads was successively chosen to be 2, 2.5 and 4 times that of the silicon carbide. For all experiments a Stokes' settling velocity model, assuming that both particles are spherical, gives a settling rate of the glass beads that is greater than that of the silicon carbide by a factor ranging from 1.6 to 16.5. When the ratio of the Stokes' settling velocity of the glass beads to that of the silicon carbide is greater than $\sim$6, we find a complete agreement between the box model and the experiment. In particular, the deposit shows a substantial decline in the mass of the coarser glass beads in the first metre, so that it only contains the finer silicon carbide further downstream. By contrast, when the Stokes' settling velocity ratio is less than $\sim$4, only the speed of the current and the total sedimented mass can be well described by the box model. The experimental deposit is otherwise characterized by a slightly increasing density, which the box model fails to match. There is no difference in the deposit density across the valley. For all experiments in the V-shaped valley, the width of the currents decreases with time t according to $t^{-2/7}$. Analogue experiments in a flat-bottom tank were also performed to assess the influence of the valley on the sedimentation dynamics described above. A similar behaviour with settling velocity ratios was found. This study eventually shows the need for considering particle interactions in even dilute gravity currents at high Reynolds numbers.

Key words: channel flow, gravity currents, sediment transport

1. Introduction

Pyroclastic and turbidity flows are both gravity currents carrying particulate matter. Deposits produced by such currents are especially important. Deposits from pyroclastic flows are the key source of information to evaluate volcanic hazards. Deposits from turbidity currents are well known for being significantly hydrocarbon-rich as well as being reservoirs of other minerals. Both currents have been the subject of much

† Email address for correspondence: cameriaux@fc.ul.pt

attention over the last few decades (see, for example, the reviews by Sparks (1976), Kneller & Buckee (2000) and Meiburg & Kneller (2010)).

Sedimentation is a key process in dilute turbidity currents and pyroclastic flows. One key feature that is expected from such dilute polydispersed currents is the sedimentation of the coarser particulate sizes upstream, whereas the finer particulate sizes settle further downstream. Such settling dynamics has been well established by laboratory experiments in long flumes driven by steady influx (e.g. Garcia 1994), or by lock-exchange experiments in which a fixed volume is initially released from a lock in a long flat-bottom tank (Gladstone, Phillips & Sparks 1998; Choux & Druitt 2002; Hodson & Alexander 2010). Several numerical models for currents consisting of one type of particulate matter but with several grain sizes showed a sedimentation behaviour similar to that observed in the laboratory studies. Although these models were based on quite distinct numerical approaches, they similarly assumed that sedimentation occurs through the basal viscous sublayer from a vertically uniform particle concentration that is well mixed by turbulence. Hence, they relied on a settling velocity in the Stokes' range. Following Garcia (1994), Salaheldina *et al.* (2000) used a layer-averaged model that incorporated water entrainment, dynamic friction, sediment exchange with the erodible bottom and an empirical equation accounting for the effects of size, density, shape and roundness on the settling velocity of natural sediments, as established by Dietrich (1982). The model described by Bonnecaze, Huppert & Lister (1996) was based on shallow-water equations, and assumed Stokes' settling. Huang, Imran & Pirmez (2007) developed a model for turbidity currents propagating down a slope using three-dimensional Reynolds-averaged Navier–Stokes equations, with a multiphase approach and a turbulence closure scheme while adopting Dietrich's fall-velocity estimate. The model includes the exchange of sediments with the bottom boundary via erosion and deposition.

In currents where particles differ not only by grain size but also by density, large and small particles could coexist in the deposit at large distances from the source when the settling velocities for the large and small particles are equivalent. This concept of hydrodynamic equivalence has, for instance, been proposed by Dade & Huppert (1996) to explain why large pumices were found together with smaller lithics at large distances downstream, in the case of the Taupo ignimbrite. In this case the settling velocity was that of particles in low-density gases, which is proportional to $(g\rho d)^{1/2}$, where g is the gravitational acceleration, ρ is the ratio of particle-to-gas phase densities and d is the size of the particle. In polydispersed dilute currents, the settling velocity is characterized by the Stokes' velocity, and the hydrodynamic equivalence would thus require $g\rho d^2$ to be similar between particles of different densities and sizes. This contrasts with the proposed criterion of a turbulent settling regime that is $\rho^2 d$, as assumed by Choux & Druitt (2002) in their analogue study of pyroclastic density currents.

Monaghan *et al.* (2009*a*,*b*) were the first to assess the extent to which the topography of a V-shaped bottom affects currents of constant volumes. In particular they found that the speed of the currents and the deposits of their monodispersed particulate currents can be described with remarkable accuracy by a box model. In addition to the valley, our study considered bidispersed particulate gravity currents as a further step in modelling more realistic currents. The objectives were to: (*a*) develop a box model for binary suspensions; and (*b*) benchmark the new box model with laboratory experiments. This paper presents the combined box model and laboratory experiments of bidispersed particulate gravity currents at high Reynolds numbers flowing along a V-shaped valley. Our study also tests the concept of hydrodynamic

equivalence discussed previously, as we consider particles of different densities and different sizes, namely silicon carbide and glass beads. Our laboratory experiments reveal that the density of the deposits as a function of distance from the point of release of the currents can be strikingly different from that predicted by the box model, which systematically follows the well-accepted trend for decreasing grain size along the current. Only when the Stokes' settling velocity ratio between the coarser and finer particles is greater than ∼6 do we retrieve agreement between the experimental data and the box model. As the Stokes' settling velocity ratio between the coarser and finer particles is less than ∼4, the density of the deposit is found to be slightly increasing, which suggests that there was quasihydrodynamic equivalence between the two particles. To check whether the valley has a major influence on sedimentation, two experiments, which were similar in grain size and initial gravitational potential energy as the V-shaped experiments, were performed in a flat-bottom geometry. We found that the final deposits have density characteristics similar to the V-shaped analogues. So the presence of the valley does not affect the sedimentation mechanisms. The box model is first described in § 2, whereas § 3 details the experiments. In § 4 we present our results from the box model and experiments. We discuss our results and present our conclusions in §§ 5 and 6, respectively.

2. The box model for a binary suspension

In this section we generalize the box model of Monaghan *et al.* (2009*a*,*b*) for binary suspensions released in lock-exchange experiments. We consider the two geometries of a current propagating over either a flat bottom or a V-shaped valley. The box model relies on three assumptions: (*a*) the velocity of the front of the current is given by a Froude number condition; (*b*) the sedimentation of the particles during the flow follows a generalized deposit formula from Martin & Nokes (1988, 1989) and Monaghan *et al.* (2009*b*); and (*c*) the volume of the current V is constant.

First, if X is the coordinate of the front measured from the origin of the lock, the velocity of the front of the current is given by

$$\frac{\mathrm{d}X}{\mathrm{d}t} = Fr\sqrt{g'h}, \tag{2.1}$$

where h is the depth of the current, $Fr \sim 1$ is the Froude number and g' is defined by

$$g' = \frac{(\rho_c - \rho_w)}{\rho_w} g, \tag{2.2}$$

where ρ_c is the density of the current, ρ_w is the density of water and g is the gravitational acceleration. In the binary suspension, the density of the current ρ_c is given by

$$\rho_c = \frac{M + m_1 + m_2}{m_1/\rho_1 + m_2/\rho_2 + M/\rho_w}, \tag{2.3}$$

where m_1 and m_2 are the masses of particles 1 and 2, the densities of which are ρ_1 and ρ_2, respectively, and M is the mass of water that is in the lock prior to the release of the current.

Second, the sedimentation of the particles during the flow is described by

$$\frac{\mathrm{d}m_i}{\mathrm{d}t} = -\gamma \frac{m_i v_s^i}{h}, \tag{2.4}$$

where m_i and v_s^i are the mass and sedimentation velocity of particles $i = 1, 2$, and γ is a parameter that was shown to be less than 1 and to vary around 0.5–0.7 for monodispersed currents (Monaghan *et al.* 2009*b*). We use an estimate of the sedimentation velocity similar to that of Monaghan *et al.* (2009*b*), which leads to

$$v_s^i = \frac{d_i^2 g(\rho_i/\rho_w - 1)(1 - \varphi_i^5)}{18\nu}, \tag{2.5}$$

where d_i is the diameter of the particles i, ρ_i is the density of the particles i, ν is the kinematic viscosity of water and φ_i is the volume concentrations of particles $i = 1, 2$ in the current, given by

$$\varphi_i = \frac{m_i}{M}\frac{\rho_w}{\rho_i}. \tag{2.6}$$

We note that using (2.4) means that the current is well mixed, as it ignores any turbulent diffusion where mass is transferred through the mixing of eddies. This would have led to an additional term that depends on the turbulent Schmidt number S_{ct}, which is the ratio of turbulent eddy viscosity to mass eddy diffusivity. Such a term is, for instance, considered in the model of Huang *et al.* (2007). Equation (2.4) can be expressed in terms of φ_i using (2.6), which gives

$$\frac{\mathrm{d}\varphi_i}{\mathrm{d}t} = -\gamma\frac{\varphi_i v_s^i}{h}. \tag{2.7}$$

Equation (2.7) means that particles of type i, and of uniform particle concentration φ_i in the current, leave the current at the viscous sublayer with the Stokes' settling velocity v_s^i, independently of particle type j.

Third, if h_0 is the initial depth of the current and L is the length of the lock, the volume condition in the case of the flat bottom at time t when the current front is at X leads to

$$h = \frac{V}{XW} = \frac{h_0 L}{X}, \tag{2.8}$$

where W is the constant width of the current.

In the V-shaped valley, the height of the current h is measured from the bottom of the valley of height a. So, when $h \geqslant a$,

$$h = \frac{a}{2} + \frac{V}{WX} = \frac{a}{2} + \frac{A}{X}, \tag{2.9}$$

where the cross-section $A = V/W$ is known from the initial volume as $A = V/W = L(h_0 - a/2)$. When $h < a$,

$$h = \sqrt{\frac{2aV}{XW}} = \sqrt{\frac{2aA}{X}}. \tag{2.10}$$

The system of equations (2.1)–(2.10) is solved numerically using a midpoint predictor–corrector algorithm. To increment the mass deposited from the current with time, the total mass deposited, $\Delta m = \Delta m_1 + \Delta m_2$, during a time step is equally distributed between strips of length Δx that divide the bottom of the tank. At a time t, the number of strips in which the deposited mass is incremented is $X/\Delta x$. If m^k is the final mass in strip k, the mass per strip area at the position of the strip is, in the presence of the valley, $m^k/(2S\Delta x)$, where $S = \sqrt{W^2/4 + a^2}$, and $m^k/(W\Delta x)$ for the flat bottom.

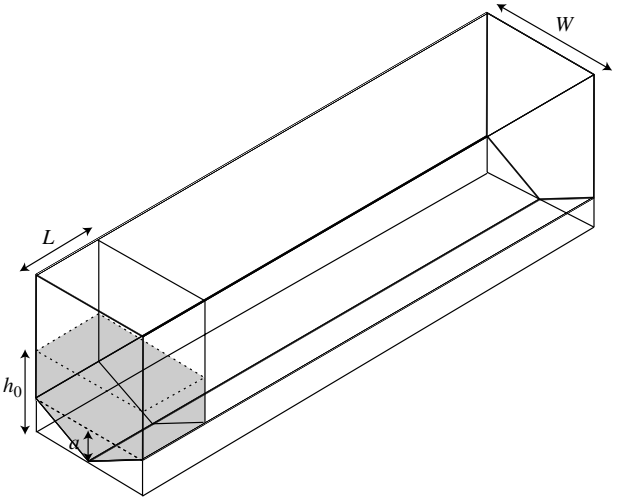

FIGURE 1. Schematic of the lock-exchange tank with inserted valley. Dimensions of W, L and a are 30, 13 and 6.65 cm, respectively. In all experiments with the V-shaped valley, h_0 was 0.126 cm, whereas h_0 was 0.120 cm for the flat-bottom experiments.

The deposited mass fraction f_1^k of particles 1 is evaluated as

$$f_1^k = \frac{m_1^k}{m_1^k + m_2^k}, \tag{2.11}$$

where m_1^k and m_2^k are the final masses of particles 1 and 2, respectively, in strip k. We then define the density of the deposit by its material density, which we will also determine experimentally. The density of the deposit ρ_d^k in strip k is thus defined by the particulate mass m^k in strip k divided by the volume occupied by the particulate matter, which gives

$$\rho_d^k = \frac{m_1^k + m_2^k}{m_1^k/\rho_1 + m_2^k/\rho_2}. \tag{2.12}$$

Equation (2.12) can further be expressed in terms of f_1^k, which gives

$$\rho_d^k = \frac{\rho_1 \rho_2}{[f_1^k \rho_2 + (1 - f_1^k)\rho_1]}. \tag{2.13}$$

3. The laboratory experiments

3.1. *Laboratory protocol*

The experiments were carried out in a Perspex rectangular tank 5 m long and 30 cm wide. We either used the flat-bottom tank or we inserted a V-shaped valley in the tank, sealed along the tank edge with transparent tape at the edges of the valley, and with transparent silicon in the lock. The V-shaped valley had a height of 6.65 cm (figure 1).

Particles of silicon carbide (SiC) and glass beads (GBs) were manually wet sieved with shaking, to select given grain sizes, until the endpoint test (i.e. when the quantity passing through the sieve in 1 min is less than 0.1 % of the total) was reached. We found that dry sieving was inappropriate, because of the presence of a significant

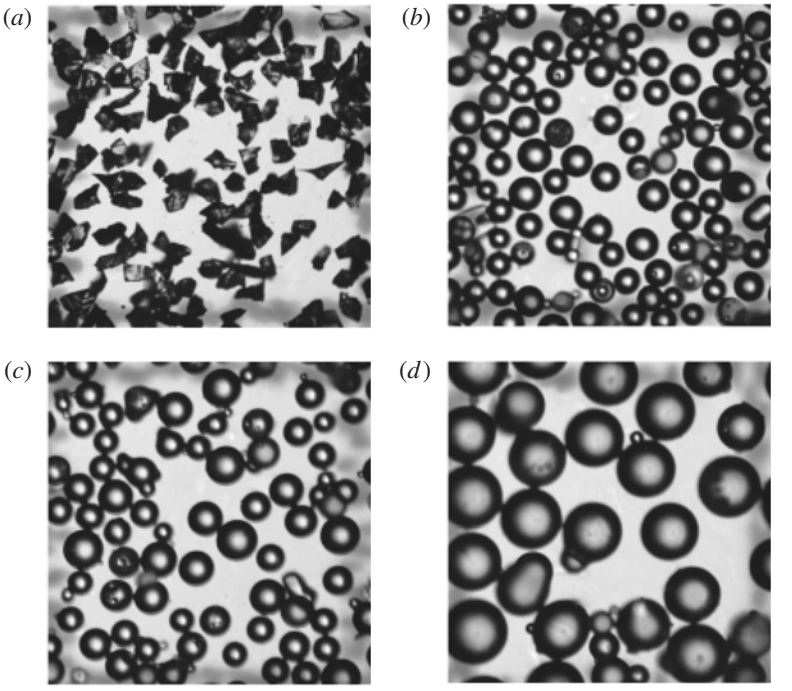

FIGURE 2. Close-up view of the SiC (*a*) and GBs (*b–d*) used for the experiments after sieving. The scale of each frame is 0.5 mm × 0.5 mm. The microscope used a magnification of 400×. Panels (*b*), (*c*) and (*d*) show sampled GBs of sizes 50–63, 60–80 and 100–125 μm. Note the contrasting shape and roundness of the smooth GB spheres and the sharp angular SiC grains.

quantity of dust in our bulk materials. Figure 2 shows samples of the grains used for the experiment after sieving.

The tank was initially filled with tap water up to a fixed depth h_0, measured from the surface of the water to the bottom. A Perspex gate with foam seal at its bottom was positioned at a fixed distance, $L = 13$ cm, from one end of the tank. A measured mass m_0 of particles composed of SiC and GBs was added to the volume of water held behind the lock gate. The mixture was stirred vigorously to bring all of the particles into suspension before the gate was rapidly lifted to release the current. Once the flow had stopped and the particles had been deposited, the tank was carefully drained. In the V-shaped valley and flat-bottom experiments, successive strips of length 25 cm were then cut over the tank width into the wet, cohesive deposits from the end of the lock to the final position of the current. In experiment 1 with the V-shaped valley (see table 1), each strip was cut into three slices consisting of two symmetric flank substrips, each of length 12 cm, and a central substrip of length 8.8 cm. Note that we never observed ripples at the surface of the deposits. Figure 3 shows a close-up view of the sampled deposit in the last strip for experiments 1, 3, 4 and 5. Remarkably, the photos reveal the presence or absence of GBs at the end of the deposit.

Each experiment was recorded by a camera in video mode. Measurements of the position of the front of the current as a function of time were obtained from frame-by-frame replay of the video recording.

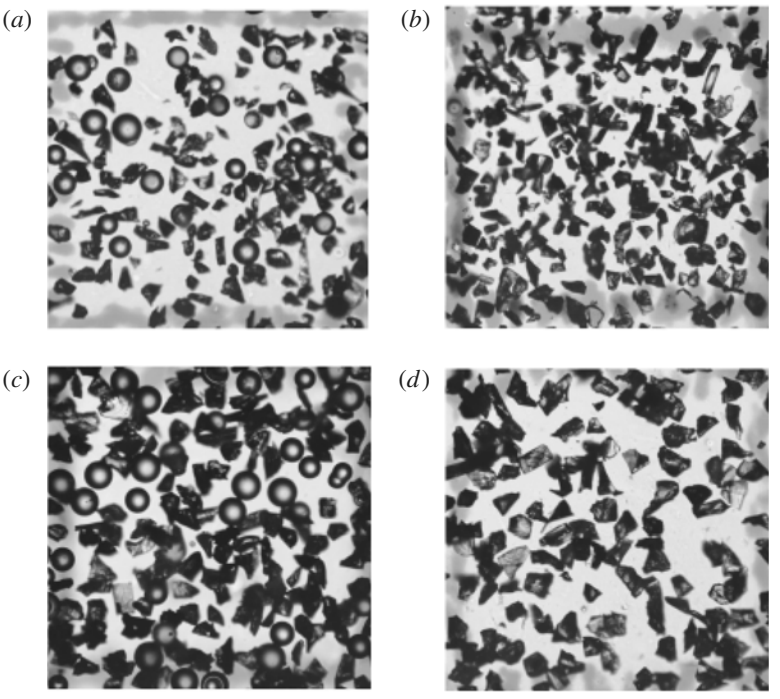

FIGURE 3. Close-up view of the sampled deposits from the last strip in experiments 1, 3, 4 and 5: panels (*a*), (*b*), (*c*) and (*d*), respectively. The scale of each frame is 0.5 mm × 0.5 mm. The magnification used was 400×. Remarkably, the photos show the presence or absence of GBs, carried or not by the current to the end. The density measurements will confirm this and further quantify the quantity of SiC and GBs in each deposit.

Experiment	Bottom	$\Delta\rho/\rho_w$ (%)	h_0 (m)	m_0^{SiC} (kg)	d_{SiC} (μm)	d_{GB} (μm)	φ_0	g_0' (m s^{-2})	Re_0	M_{lock} (%)
0	V-shaped	0.0443	0.126	0.238	25–32	—	0.0205	0.4344	29 566	10.5
1	V-shaped	0.0443	0.126	0.130	25–32	50–63	0.0263	0.4346	29 484	13.4
2	V-shaped	0.0443	0.126	0.130	25–32	63-80	0.0263	0.4346	29 484	13.8
3	V-shaped	0.0443	0.126	0.130	25–32	100–125	0.0263	0.4346	29 484	29.2
4	Flat	0.0451	0.120	0.168	25–32	50–63	0.0258	0.4422	27 644	20.3
5	Flat	0.0451	0.120	0.168	25–32	100–125	0.0258	0.4422	27 644	31.5

TABLE 1. Initial experimental conditions. The initial Reynolds number is estimated following $Re_0 = \sqrt{g_0' h_0^3/\nu^2}$, where the kinematic viscosity of water ν is 10^{-6} m^2 s^{-1}. The variable φ_0 is the total initial volume concentration of the particles. We note that the initial mass of the glass beads m_0^{GB} was equal to that of the silicon carbide m_0^{SiC} in all experiments, except for experiment 0, which was performed with SiC only. The initial loss of mass in the lock M_{lock} is given as a percentage relative to the total initial mass m_0^{SiC} or $m_0^{GB} + m_0^{SiC}$. The variable $\Delta\rho$ is $(\rho_c - \rho_w)$.

3.2. *Analysis of the deposits*

The particles in each strip were collected in a beaker and then dried and weighed. The particles that had remained in the lock were also collected and weighed. Density measurements of the particulate matter within each beaker were then made using calibrated pycnometers and ultrapure water. Four density measurements were performed for each beaker from four subsamples of the total mass, except for the beaker that contained the deposit from the end of the current. As this beaker contained just a small amount of deposit, the four estimates were obtained by repeating the measurements from the same mass. The content of each beaker was thoroughly mixed before taking the four subsamples. Depending on the mass available, we used pycnometers of volumes 100, 50 and 25 ml. From a calibration study with pure SiC, we identified that our density estimates had errors $\leqslant 4\,\%$ when using a mass of 10 g and the 100 ml pycnometers, but within $12\,\%$ when using only 2 g. For the 50 ml pycnometers, the error was $3\,\%$ when using a mass of 10 g, but the error rose to $8\,\%$ when using only 2.5 g. For the 25 ml pycnometers, the error was $3\,\%$ when using a mass of 5 g but $15\,\%$ when using only 2.5 g.

These measurements enable us to characterize the density of the particulate matter as defined by (2.12). For a pycnometer of volume V_p, the mass of water m_{pw} is $V_p\rho_w$. When particles of total mass m_s^i of the sampled strip i are placed in the pycnometer, they occupy by definition a volume m_s^i/ρ_d^i, where ρ_d^i is the material density of the deposit of the ith sampled strip. As the pycnometer is then filled with water up to the level marking its volume of calibration, the total mass m_{pwg}^i is $m_{pwg}^i = m_s^i + \rho_w(V_p - m_s^i/\rho_d^i)$. Consequently, the density of the deposit of the ith sampled strip ρ_d^i is given by

$$\rho_d^i = \rho_w \frac{m_s^i}{m_s^i + m_{pw} - m_{pwg}^i}, \tag{3.1}$$

where m_s^i, m_{pw} and m_{pwg}^i are all measured quantities. Having determined the density of the deposit strip sample ρ_d^i, the mass fraction f_1^i of particles 1 in strip i can be calculated using (2.13) and, knowing the mass of particles $(m_1^i + m_2^i)$ in strip i, the mass of particles m_1^i and m_2^i in strip i can be calculated using (2.11).

We note that the deposit density ρ_d represents a material density of the deposit, which shows the granular composition of the deposit. The quantity ρ_d differs from the *in situ* density of the deposit. First, ρ_d does not depend on the arrangement of the grains in the granular bed, which includes the voids between grains. Second, ρ_d cannot provide any information on the stratification of the deposits, which are thought to develop for particulate currents with small initial concentrations (McCaffrey *et al.* 2003). For suspensions of highly polydispersed particles with concentrations of 13.8–23.0 % by volume, deposits are strongly stratified (Choux, Druitt & Thomas 2004). Our deposits were too thin (just a few millimetres at the lock gate) for us to look at the vertical structure of the deposits.

3.3. *Initial conditions of the laboratory experiments*

Prior to the experiments presented in this paper, we carried out a number of tests to assess our laboratory methodology. In particular, we found that the final position of the front was critically linked to the degree to which our sieving had selected the desired grain size. Although not contributing to the deposit, a tiny fraction of dust or finer grain sizes were responsible for the current stopping tens of centimetres further downstream. Here we present six selected experiments, four of which were performed

Experiment	v_s^{SiC} ($\times 10^{-3}$) (m s^{-1})	v_s^{GB} ($\times 10^{-3}$) (m s^{-1})	v_s^{GB}/v_s^{SiC}	v_{sc}^{SiC} ($\times 10^{-3}$) (m s^{-1})	v_{sc}^{GB} ($\times 10^{-3}$) (m s^{-1})	v_{sc}^{GB}/v_{sc}^{SiC}
0	0.71–1.16	—	—	0.56-0.92	—	—
1	0.71–1.16	1.88–2.98	1.62–4.21	0.56–0.92	1.76–2.80	1.90–4.96
2	0.71–1.16	2.98–4.80	2.57–6.79	0.56–0.92	2.80–4.51	3.02–7.99
3	0.71–1.16	7.51–11.73	6.48–16.59	0.56–0.92	7.05–11.02	7.62–19.51
4	0.71–1.16	1.88–2.98	1.62–4.21	0.56–0.92	1.76–2.80	1.90–4.96
5	0.71–1.16	7.50–11.72	6.48–16.58	0.56–0.92	7.05–11.01	7.62–19.51

TABLE 2. Initial sedimentation velocities for the SiC and GB particles, v_s^{SiC} and v_s^{GB}, respectively, within their grain size ranges in each experiment, as indicated in table 1. Velocities are calculated according to (2.5). In all experiments, the GBs are expected to sediment faster than the SiC particles within velocity ratios that range from a factor of 1.62 to a factor of 16.48. v_{sc}^{SiC} and v_{sc}^{GB} are the settling velocities corrected for viscosity, and for the shape and roundness of particles, as discussed in § 5.4.

in the V-shaped valley and two of which used the flat-bottom tank. Experiment 0 was a monodispersed gravity current made of SiC in the V-shaped valley that is used for comparison with the bidispersed currents of experiments 1–3. Details of the initial conditions for the currents are given in table 1. In all experiments, the volume fraction of particles was small, and imposed an initial density of the current of 4 % higher than that of water. The V-shaped experiments 1–3 only differed in the grain size of the GBs, ranging from 50–63 to 100–125 μm in diameter. The SiC particle grain sizes were kept within the range 25–32 μm in diameter. The densities of SiC and GBs were measured three times, and were (3188 ± 33) and (2475 ± 12) kg m^{-3}, respectively. Table 2 gives the corresponding initial sedimentation velocities for the SiC and GB particles, following (2.5).

The initial conditions of flat-bottom experiments 4 and 5 were chosen so that their initial gravitational potential energy equalled that of V-shaped experiments 1 and 3, respectively. This constraint is achieved by having $h_{0(Flat)}^2 = h_{0(Valley)}^2 - 1/3a^2$. The flat-bottom experiments were carried out to assess the role of the valley in sedimentation. The particle loss in the lock was greater (see table 1) than that described by Monaghan *et al.* (2009*b*), which was 5–10 % of the initial mass, because of the larger grain sizes used in this study.

4. Experimental and box model results

4.1. *The box model runs*

The numerical code was first checked against the experimental data and results of the box model of Monaghan *et al.* (2009*b*). The tests were simply performed by setting the properties of SiC and GB particles to be equal, and their initial masses to be half of those used in the experiments of Monaghan *et al.* (2009*b*). Full agreement was found in this comparison exercise. The input masses m_0^{SiC} and m_0^{GB} used in the box model were actually not exactly those indicated in table 1. As the loss in the lock was greater than 10 % of the initial mass (see table 1), we applied a correction to the initial masses m_0^{SiC} and m_0^{GB} for the box model. Given the smaller grain size of SiC relative to the GBs, it was expected that the deposit in the lock would contain more GBs than SiC. The mass concentration of SiC in the lock deposit was thus determined from the

Experiment	ρ_{lock} (kg m^{-3})	m_0^{SiC} (kg)	m_0^{GB} (kg)	γ	t^{α}	MAE	$X_R^e \pm 0.05$ (m)	X_R^b (m)
0	(3188±33)	0.213	—	0.9	$t^{-0.32}$	0.0043	3.80	3.77
1	(2714±38)	0.116	0.109	0.8	$t^{-0.29}$	0.0062	3.55	3.57
2	(2680±14)	0.116	0.108	0.9	$t^{-0.27}$	0.0069	3.10	3.26
3	(2660±04)	0.106	0.078	0.9	$t^{-0.27}$	0.0071	3.03	3.12
4	(2694±14)	0.143	0.125	0.4	—	—	2.65	2.72
5	(2603±04)	0.144	0.081	0.5	—	—	2.30	2.42

TABLE 3. Corrected mass inputs for the box model, best fit γ factor, narrowing width functions t^{α}, mean absolute errors (MAEs) for the linear regressions, experimental and box model run-out lengths X_R^e and X_R^b, respectively.

measure of the density of the deposit in the lock ρ_{lock}, using (2.13). Table 3 gives the resulting corrected masses of SiC and GBs that were used to run the box model. We also used the average values between the minimum and maximum particle sizes indicated in table 1 to run the box model. The strips were set to a length $\Delta x = 0.05$ m in all runs. Finally, table 3 indicates the value of γ that leads to the best fit between the box model and the experimental data. We note that the Froude number Fr was always taken as being equal to 1 in all of the runs.

4.2. *V-shaped geometry*

4.2.1. *Front of the current with time and total mass deposited*

Figure 4 shows the variation of the position of the head of the current against time for experiments 1–3 in comparison with experiment 0. The agreement between the box model results and the experimental results is good. As the grain size of the GBs is increased, the bidispersed currents flow at increasingly slower speeds compared with the monodispersed current. This is as expected because larger particles are more rapidly lost from the currents because of their larger settling rates, which results in a decrease of the driving effective gravity. Figure 5 shows the experimental data and the box model results for the total mass deposited per area as a function of distance x along the tank for experiments 0–3. The agreement between theory and experiment for the total mass deposited is good. The difference in the mass deposit across the valley is shown for experiment 1 in figure 6. The overall match between the measured data and the simulated results is not as good as for the total mass. Compared with the experimental data, the box model overestimates the mass deposited in the flanks, whereas it underestimates the deposited mass in the central region of the valley. However, both show that there is a factor of 4–5 difference in the magnitude of the mass per area in the central region compared with that on the flanks of the valley. Such variation has already been described for monodispersed currents (Monaghan *et al.* 2009*b*), and has been explained by the inability of currents to deposit on flanks while flowing along the narrowing valley.

4.2.2. *Deposit density*

Figure 7 shows the density of the deposit for experiments 1–3 as determined from the experimental data and box model runs. For experiment 1, panel (*a*) shows the density determined from the substrips collected in the central part of the valley and on the flanks. A good agreement between the experimental and box model results is found for experiment 3 only (panel *c*). In particular, the deposit density determined

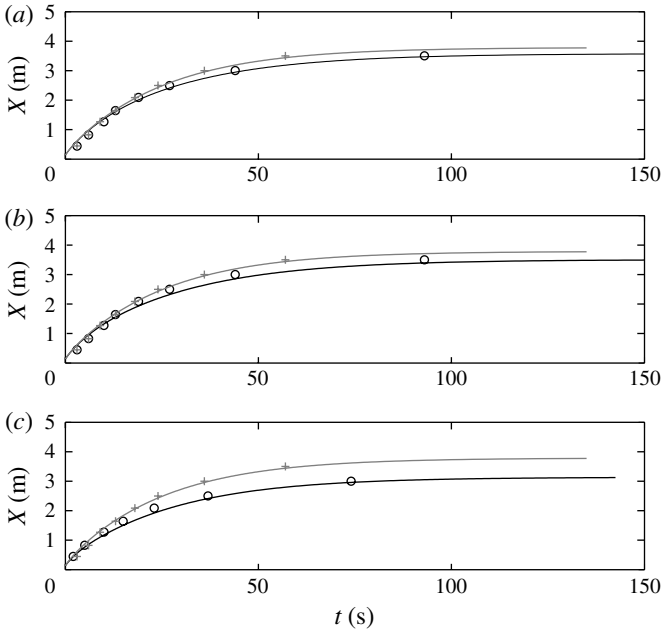

FIGURE 4. Position of the head of the current $X(t)$ (m) as a function of time t (s). Panels (*a*)–(*c*) show the bidispersed experiments 1–3 of table 1. The black straight lines and black circles are the box model results and the experimental data, respectively. In all frames, the monodispersed experiment 0 is shown for comparison as grey solid lines and grey crosses, representing the box model results and experimental data, respectively.

in experiment 3 at the end of the current matches together with the box model that of SiC. By contrast, results from experiment 1 (panel *a*) and 2 (panel *b*) agree with the box model results in the first metre of the deposit only. The experimental data of experiment 1 suggest a deposit of slightly increasing density (6.8 %) along its length that is not predicted by the box model, for which density increases all along the length to equal the density of SiC at the end of the deposit. There is no difference that can be seen between the experimental density across the valley, as the density within the central region and the flanks are similar. This supports the assumption of a current well mixed by turbulence. Compared with experiment 1, the data in experiment 2 show a larger increase in deposit density as the distance increases from the lock position, but they still indicate the presence of glass beads at the end of deposit, as also illustrated in figure 8, which shows the volume concentration of SiC in the deposit for the three experiments. The mass deposition misfit between the experimental data and the box model results can also be seen when the masses deposited for both SiC and GBs in the experiments are back-calculated from the measured deposit density, as shown in figure 9 for experiment 1.

4.2.3. *Widths of the currents*

Figure 10 shows the widths predicted by the box model for gravity currents of experiments 0–3 as the head of the currents is at $X = 1.64$ m. The current width values calculated with the box model are in good agreement with the experiments. The predicted current front position in panels (*c*) and (*d*) is ∼10 cm less than the actual front position of the current, which is explained by the slightly slower speed predicted

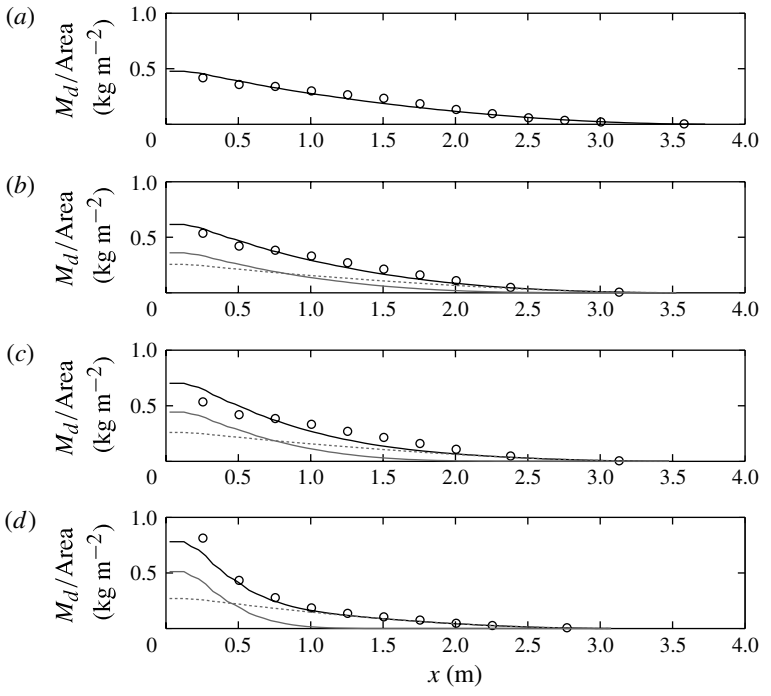

FIGURE 5. Mass deposited per strip area M_d/Area (kg m^{-2}) as a function of distance x (m). Panel (a) corresponds to monodispersed experiment 0 of table 1, whereas panels (b–d) correspond to bidispersed experiments 1–3. The black straight lines and black circles represent the box model predictions and experimental data for the total mass deposited, respectively. The grey straight lines represent the mass deposited by the GBs, and the grey dashed lines represent the mass deposited by SiC, as predicted by the box model.

by the box model in the first 2 m of the current (see figure 4). As currents narrow when they flow along the valley, the evolution of the width of the currents is further examined with the box model. We analysed the predicted current widths over a time interval where the current front position is between 8 and 20 times the lock length. We found that the width as a function of time is very well represented by a power law of the form $t^{-\alpha}$. Table 3 gives the α coefficients obtained by linear regressions from the natural logarithm of the width versus the natural logarithm of time, a quality indicator of the fits and the mean absolute errors (MAEs).

4.3. *Flat-bottom geometry*

Two experiments were conducted in the flat-bottom tank to assess the influence of the valley. Importantly, those two experiments were analogue in terms of grain sizes with experiments 1 and 3. As for the experiments with the V-shaped valley, a good agreement between the box model and the experiments can be found in the experiments with the flat bottom for the speed of the front (figure 11) and the mass deposited per unit area as a function of distance x along the tank (figure 12). We note that the agreement between theory and experiment is much better in the V-shaped case than in the flat-bottom geometry for the mass deposited. This feature was already observed in Monaghan *et al.* (2009*b*) for monodispersed turbulent gravity currents. These results are very similar to those presented by Bonnecaze *et al.* (1996)

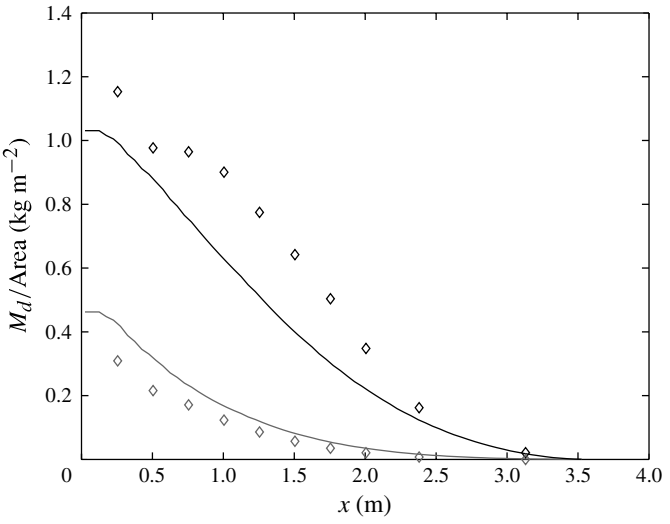

FIGURE 6. Mass deposited per strip area M_d/Area (kg m^{-2}) as a function of distance x (m) for experiment 1 in the central region of the valley and its flanks. Strips were cut into three slices consisting of two symmetric flank substrips, each of length 12 cm, and a central substrip, of length 8 cm. The experimental results are shown by diamonds and the continuous curves are the values predicted by the box model. The black upper curve and black diamonds show the results for the central region, and the grey lower curve and grey diamonds show the results for the two flanks.

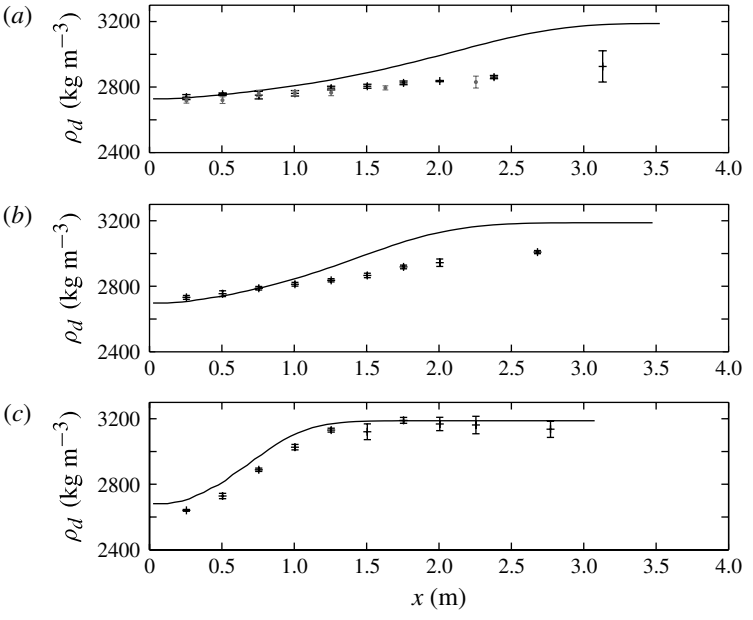

FIGURE 7. Density of the deposit ρ_d (kg m^{-3}) as a function of distance x (m). Panels (a–c) correspond to experiments 1, 2 and 3 of table 1. The straight lines represent the predictions of the box model. The crosses, with error bars corresponding to the standard deviations, are from the experimental data. Panel (a) shows the density found for the substrips of the central region (in black) and flanks (in grey) of the valley.

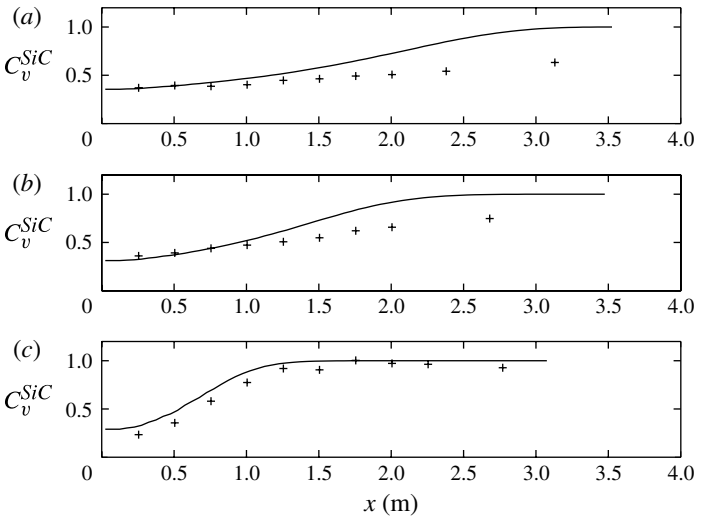

FIGURE 8. Volume concentration of SiC in the deposit $C_v^{SiC} = (\rho_d - \rho_{GB})/(\rho_{SiC} - \rho_{GB})$, as a function of distance x (m). Panels (a–c) correspond to experiments 1–3 of table 1. The straight lines represent the predictions of the box model. The crosses are from the experimental data.

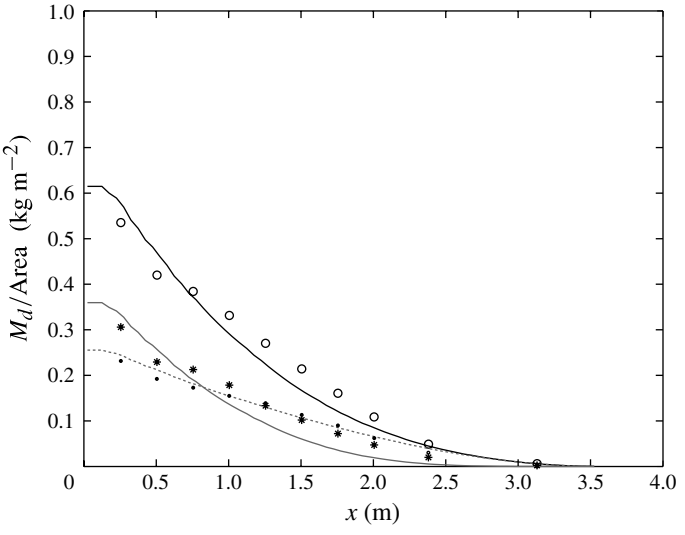

FIGURE 9. Mass deposited per strip area M_d/Area (kg m^{-2}) as a function of distance x (m) for experiment 1. The black straight line represents the total mass deposited, as predicted by the box model. The circles are the experimental total mass data. The straight grey line represents the mass deposited by the GBs and the dashed grey line represents the mass deposited by SiC, as predicted by the box model. The dots are the SiC masses deduced from the density measurements of the deposits and the stars are the GB masses deduced from the density measurements of the deposits. The factor γ was 0.8 for both particles.

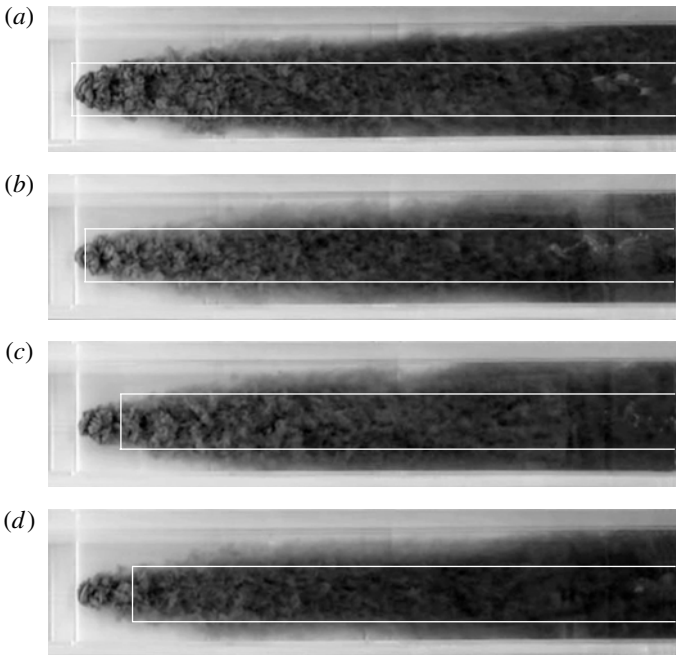

FIGURE 10. The gravity current of experiments 0–3 (panels *a–d*, respectively), seen from above when the head of the current is $X = 1.64$ m. The views show the currents from the end of the lock, so the current length shown in all frames is 1.51 m. The width of the tank of 30 cm seen from above is used to scale the widths. The white lines show the boundaries of the box model. The width of the boxes calculated with the box model are in good agreement with the experiments. For experiments 2 and 3, the front calculated by the box model is slightly less than the experimental one, which is also seen in the fits found for the front position of the currents as a function of time (figure 4).

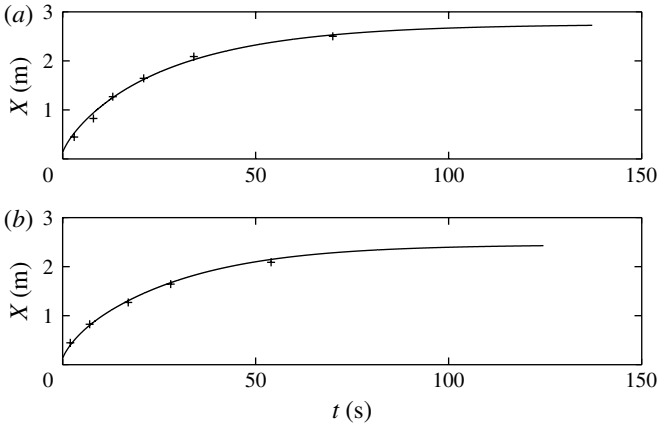

FIGURE 11. Position of the head of the current $X(t)$ (m) as a function of time t (s). Panels (*a*) and (*b*) correspond to experiments 4 and 5 of table 1. The straight lines represent the box model and the crosses represent the experimental data.

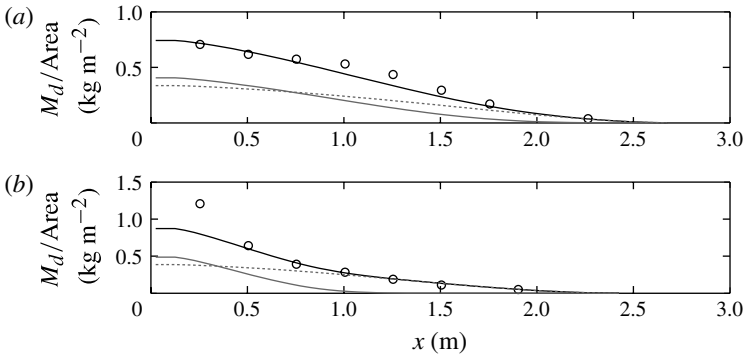

FIGURE 12. Mass deposited per strip area M_d/Area (kg m^{-2}) as a function of distance x (m). Panels (*a*) and (*b*) correspond to experiments 4 and 5 of table 1. The straight lines represent the total mass deposited as predicted by the box model and the circles are the experimental data. The straight grey lines represent the mass deposited by the GBs and the dashed grey lines represent the mass deposited by SiC, as predicted by the box model.

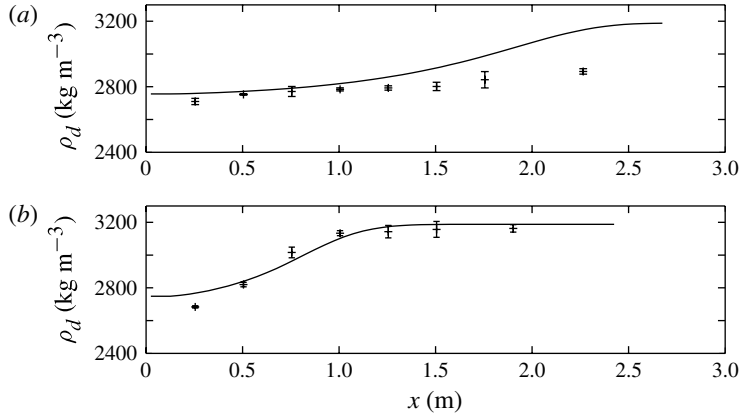

FIGURE 13. Density of the deposit ρ_d (kg m^{-3}) as a function of distance x (m). Panels (*a*) and (*b*) correspond to experiments 4 and 5 of table 1. The straight lines represent the predictions of the box model. The crosses, with error bars corresponding to standard deviations, are from the experimental data.

for polydispersed turbidity currents. On the other hand, there is again disagreement between the box model results and the experimental data for the deposit density in experiment 4 (figures 13*a* and 14*a*). The density shown by the experimental data shows a slight increase of 6.8 %, similar to that observed in experiment 1 in the V-shaped valley. By contrast, good agreement between the experimental and box model results is found for experiment 5 (figures 13*b* and 14*b*), as in the case of experiment 3.

5. Discussion

5.1. *Run-out distance of currents in the V-shaped valley*

The run-out distances of particulate currents depend on the settling rate of the particles. As the loss of particles from a current results in a decrease of its driving effective

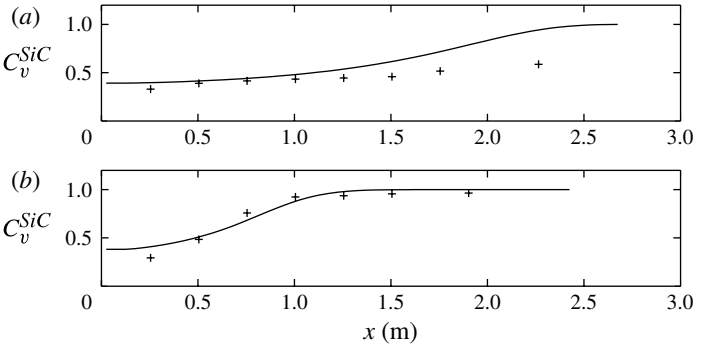

FIGURE 14. Volume concentration of SiC in the deposit $C_v^{SiC} = (\rho_d - \rho_{GB})/(\rho_{SiC} - \rho_{GB})$ as a function of distance x (m). Panels (a) and (b) correspond to experiments 4 and 5 of table 1. The straight lines represent the predictions of the box model. The crosses are from the experimental data.

gravity, a current in which particles settle at a slow rate may travel a few times the distance of a current in which particles sediment quickly. Gladstone *et al.* (1998) showed such a relationship in studying constant-volume gravity currents consisting of two sizes of SiC (25 and 69 μm) and flowing in a flat-bottom tank. In this study, we found that the run-out lengths resulting from currents flowing along the valley are 35 % higher than those of currents flowing along a flat bottom (see table 3). This probably results from the larger initial velocity of the current in the case of the V-shaped valley because, for equal initial gravitational potential energy, the height of the fluid h is less for the flat-bottomed tank (see § 3.3). However, run-out lengths vary in the same way with the grain size distribution in the V-shaped and flat-bottomed geometries. Comparison of the run-out lengths for experiments 1 and 3 in the V-shaped valley, and for experiments 4 and 5 with the flat bottom, shows a similar decrease of the run-out lengths with increasing GB grain size. The run-out length decreases by 14.6 % in the V-shaped valley and by 13.2 % with the flat bottom, which is similar.

5.2. *Widths of the currents*

An obvious but significant feature of the flows along the valley is that currents narrow with time. In the case of saline gravity currents, Monaghan *et al.* (2009*a*) showed from a similarity solution that, for sufficiently long lengths of time, the width of the current decreases with time as $t^{-2/5}$. Good agreement was found with the experiments. In the case where the deposition of particles occurs during the flow, this study shows that the particulate currents narrow a little less with time, as $\sim t^{-2/7}$ for particulate currents. No significant statistical difference could be found in the α values between the monodispersed and bidispersed currents (table 3).

5.3. *Effect of the V-shaped valley on the deposit density*

Monaghan *et al.* (2009*a*,*b*) showed that the presence of the valley had a major impact on saline and monodispersed gravity currents, compared with those flowing along a flat bottom. Currents are then characterized by, for instance, a parabolic front with radius of curvature proportional to the initial depth of the current, and a narrowing width with time. Not surprisingly, the same features were observed in the bidispersed currents of this study. Yet, by contrast, our study shows that the presence of the

valley does not affect the sedimentation mechanisms: bidispersed currents flowing either along the flat bottom or in the V-shaped valley, with similar grain sizes and initial driving effective gravity, resulted in either a slightly increasing deposit density (experiments 1 and 4) or an early and substantial loss of the glass beads within the first metre of the current (experiments 3 and 5).

5.4. *Sedimentation dynamics*

Our experimental results on the deposit density show that the box model does not always predict the sedimentation dynamics in the bidispersed currents. Whereas agreement can be found between the box model and experiments 3 and 5, the granular characteristics of the deposits of experiments 1, 2 and 4 are not predicted by the model. These findings indicate a need for revisiting the deposition formulae (equation (2.7)).

First, the Stokes' velocity model (equation (2.5)) can be corrected for viscosity, and for the shape and roundness of particles. For the viscosity correction, Einstein (1906) predicts an increase of the viscosity for dilute suspensions that follows

$$\mu_{suspension} = \mu(1 + k\varphi), \tag{5.1}$$

where k is the Einstein coefficient (=2.5), φ is the volumetric concentration of particles, $\mu_{suspension}$ is the total viscosity and μ is the viscosity of the interstitial fluid. Given our volumetric concentrations, the increase in the viscosity of our medium would be 6 %, leading to an ∼6 % reduction in the settling velocity of both SiC and GBs.

For the shape and roundness correction, figure 2 shows that the SiC grains depart from smooth grains, in contrast to the GBs. So only the settling velocity of SiC needs a shape and roundness correction factor. Although quantifying such a factor is somewhat conjectural, Clift, Grace & Weber (1978) showed that the velocity should be corrected by a factor K that ranges between 0.3 and 0.5 for long and thin structures, whereas it takes the value 1 for spheres. The empirical formulae of Dietrich (1982), which Salaheldina *et al.* (2000) and Huang *et al.* (2007) used for their models, gives a correction factor here for the settling of smooth spheres of $K = 0.85$. This estimate approximates the Corey shape factor (CSF), $CSF = 0.63$, and assumes a roughness factor $P = 2$ for crushed sediments. We note that the CSF is defined by $CSF = c/\sqrt{ab}$, where a, b and c are the longest, intermediate and shortest particle axes. Here we used its two-dimensional analogue from our photos (i.e. $CSF = c/a$). Overall the shape and roundness corrections for the SiC add together with the viscosity factor to decrease the SiC settling velocity by a factor 0.8.

Now, if we apply the conservative corrections for the settling velocities of 0.8 and 0.94 for SiC and GBs, respectively, in (2.5), not a single γ factor results in improved fitting. We can show improved fits of the box model against experiments 1 or 4 if we arbitrarily use different γ factors for the SiC and the GBs. For instance, figure 15 shows good agreement for the velocity of the current for experiment 1 and the box model, in which two γ fitting factors, one for SiC and a second for the GBs, were used. In addition, figure 16 shows the predicted masses deposited when using the two γ fitting factors. When compared with figure 9 based on the box model using the single best-fit value of γ for experiment 1 (see table 3), the use of two γ factors shows an improved agreement between the box model and the experiment. The density profile predicted by the box model is also better, as shown in the insert of figure 16. Table 4 shows the improvement of the fitting with the mean absolute errors calculated between the observed and simulated data. Unexpectedly, the values of the two γ

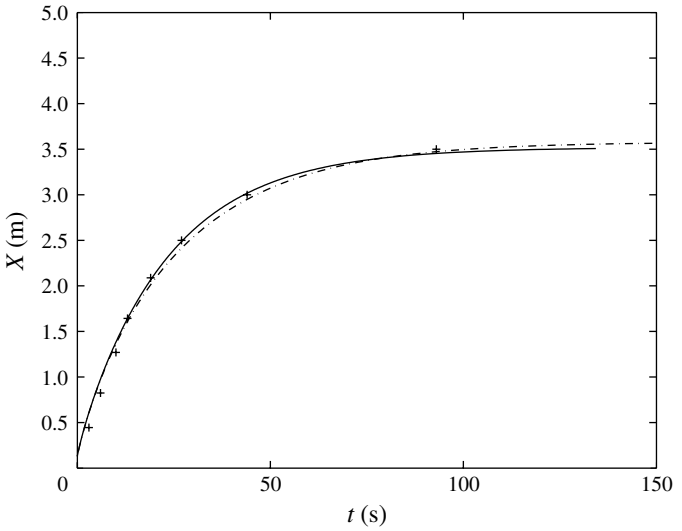

FIGURE 15. Position of the head of the current $X(t)$ (m) as a function of time t (s) for experiment 1. The straight line represents the predictions of the box model with a single value of γ of 0.8. The dashed-dotted line represents the box model with values of γ equal to 0.5 for the GB particles and 0.9 for the SiC particles. The crosses are from the experimental data.

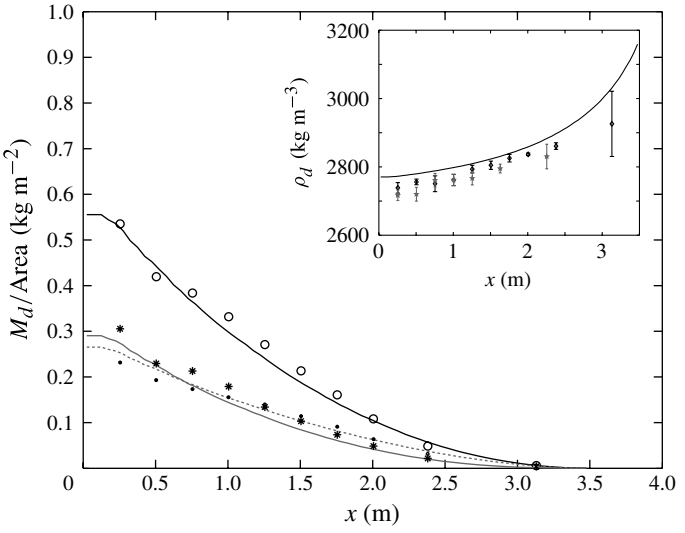

FIGURE 16. Mass deposited per strip area M_d/Area (kg m^{-2}) as a function of distance x (m) for experiment 1. The straight line represents the total mass deposited as predicted by the box model, and the circles are the experimental total mass data. The straight grey line represents the mass deposited by the GBs and the dashed grey line represents the mass deposited by SiC, as predicted by the box model. The dots are the SiC masses deduced from the density measurements of the deposits, and the stars are the GB masses deduced from the density measurements of the deposits. The factor γ was 0.5 for the GB particles and 0.9 for the SiC particles. The insert shows the improved fit of the box model for the deposit density compared with figure 7(*a*).

	X	M_d/Area	m_{SiC}/Area	m_{GB}/Area	ρ_d
MAE (1 factor γ)	0.0841	0.0305	0.0078	0.0423	0.0958
MAE (2 factors γ)	0.0662	0.0172	0.0095	0.0152	0.0343

TABLE 4. MAEs between the experimental data of experiment 1 and the box model results that have been interpolated at the same x-axis position as the experimental data for the fits based on: (*a*) a single value of γ; and (*b*) two values of γ, as discussed in § 5.4. The analysis is made for the front position X, the total mass deposited per area M_d/Area, the mass of SiC per area m_{SiC}/Area, the mass of GB per area m_{GB}/Area and the density ρ_d, as shown in figures 9, 15 and 16. The MAE values show the overall improvement of the fits with the two values of γ.

factors results in an apparent reduction of the sedimentation rate by a factor of 1.6 for the GBs, and an increase by a factor of 1.125 for SiC.

At this point there appears to be a need to go beyond simple corrections, and consider particle interactions. There are actually two types of particle interaction that could be involved here.

The first is the interaction between particles and turbulence. This could result in preferential concentrations of particles (Wang & Maxey 1993; Eaton & Flessler 1994). Settling of particles in turbulence is thought to be controlled by the Stokes' number of the particle species, i.e. the time ratio of particle response to the Kolmogorov scale of turbulence, or equivalently the ratio of particle settling velocity to upward-directed components of turbulent velocity. Only when this ratio is less than unity can the current have a vertically well-mixed distribution of the suspension load. So coarser particles could not be well mixed (see figure 6 of Garcia (1994), for steady currents). Yet, for the coarsest grain sizes of GBs (experiment 3), the box model with its assumption of a well-mixed current, and consequently a vertically uniform particle concentration, is fully satisfactory. So it is possible that the assumption of the vertical uniform particle concentration used in the equation for deposition could remain a reasonably good approximation, even in the case of small-scale and intermittent preferential concentrations, as described by Baas *et al.* (2005).

The second type of particle interaction is the interaction between the particles in the viscous sublayer. This would result in a complex correction to the settling rate, as proposed by Batchelor (1982). The formula for the settling rate is then a function of pair interactions between particles, i.e. $v_s^i = [v_s^i]_0(1 + \sum_{j=1}^{m} S_{ij}\varphi_j)$, where $[v_s^i]_0$ is the Stokes' velocity for an isolated particle of type i, the factor S_{ij} is a function of the size ratio d_j/d_i of particles of type i and j, with reduced density ratio $(\rho_j - \rho)/(\rho_i - \rho)$, Péclet number of the relative motion of particle i and particle j, and some dimensionless measure of the interparticle force potential. For suspensions containing more than one particle species, Davis & Acrivos (1985) showed that the settling rate differs significantly from the Stokes' prediction, even when the total volume fraction of particles exceeds only $\sim$1 %. Yet whether or not this would be relevant to the thin viscous sublayer remains an open question.

Undoubtedly this study motivates further investigations on particle interactions in gravity currents at high Reynolds numbers.

6. Conclusion

We have presented a study of particulate gravity currents made of SiC and GBs flowing along a V-shaped valley and a flat bottom. The speed and width of the currents, the mass deposited by the currents and the density of the deposits were examined together by a box model and lock-exchange experiments in a 5 m long tank. In all experiments the Stokes' settling velocity of the GBs was greater than that of the SiC within a factor ranging from 1.6 to 16.5. When the ratio of the settling velocity of the GBs to that of the SiC is greater than about 6, we find a complete agreement between the box model and the experiment. In particular, the deposit shows a substantial decline in the mass of the coarser GBs in the first metre, so that it only contains the finer SiC further downstream. By contrast, when the settling velocity ratio is less than $\sim$4, the experimental deposit is characterized by a slightly increasing density, which the box model fails to match unless different sedimentation γ factors are used for the SiC and the GBs. The SiC and GBs appear to be in quasihydrodynamic equivalence, which was not expected given their distinct Stokes' settling velocities. There is no difference in the deposit density across the valley. A similar dynamics of the sedimentation is found for the experiments that were performed in a flat-bottom tank. Run-out lengths vary in the same way with the grain size distribution in the V-shaped and flat-bottom geometry. So, whatever the sedimentation mechanisms involved in the deposition that produce the characteristic deposit density, they are not influenced by the presence of the valley. In all experiments in the V-shaped valley, the width of the currents decreases with time t according to $t^{-2/7}$. This study eventually showed the need for considering particle interactions in even dilute gravity currents at high Reynolds numbers.

Acknowledgements

C.A.M. thanks Plásticos Campo Grande, LDA, for their professionalism in building the tank, and J.L.P. Duarte for his help in setting the experiments. C.A.M. is grateful to Professor J. Monaghan and Dr M. Teixeira for their comments on an early draft of this paper. C.A.M. thanks an anonymous referee for his constructive remarks. Both C.A.M. and C.B.K.-B. are funded by the Ciências 2009 programme of the Fundaçao para a Ciência e a Tecnologia (FCT, Portugal). The present work was supported by the FCT under Project Pest-OE/CTE /LA0019/2011-2012.

REFERENCES

BAAS, J. H., MCCAFFERY, W. D., HAUGHTON, P. D. W. & CHOUX, C. 2005 Coupling between suspended sediment distribution and turbulence structure in a laboratory turbidity current. *J. Geophys. Res.* **110**, doi:10.1029/2004JC002668.

BATCHELOR, G. K. 1982 Sedimentation in a dilute polydisperse system of interacting spheres. Part 1. General theory. *J. Fluid Mech.* **119**, 379–408.

BONNECAZE, R. T., HUPPERT, H. E. & LISTER, J. R. 1996 Patterns of sedimentation from polydispersed turbidity currents. *Proc. R. Soc. Lond.* A **452**, 2247–2261.

CLIFT, R., GRACE, J. R. & WEBER, M. E. 1978 *Bubbles, Drops and Particles*. Academic.

CHOUX, C. M. & DRUITT, T. H. 2002 Analogue study of particle segregation in pyroclastic density currents, with implications for the emplacement mechanisms of large ignimbrites. *Sedimentology* **49**, 907–928.

CHOUX, C., DRUITT, T. & THOMAS, N. 2004 Stratification and particle segregation in flowing polydisperse suspensions, with applications to the transport and sedimentation of pyroclastic density currents. *J. Volcanol. Geotherm. Res.* **138**, 223–241.

DADE, W. B. & HUPPERT, H. E. 1996 Emplacement of the Taupo ignimbrite by a dilute turbulent flow. *Nature* **381**, 509–512.

DAVIS, R. H. & ACRIVOS, A. 1985 Sedimentation of noncolloidal particles at low Reynolds number. *Annu. Rev. Fluid Mech.* **17**, 91–118.

DIETRICH, W. E. 1982 Settling velocity of natural particles. *Water Resour. Res.* **18**, 1615–1626.

EATON, J. K. & FLESSLER, J. R. 1994 Preferential concentration of particles by turbulence. *Intl J. Multiphase Flow* **20**, 169–209.

EINSTEIN, A. 1906 A new determination of the molecular dimensions. *Ann. Phys.* **19** (2), 289–306.

GARCIA, M. H. 1994 Depositional turbidity currents laden with poorly sorted sediment. *J. Hydraul. Engng ASCE* **120**, 1240–1263.

GLADSTONE, C., PHILLIPS, J. C. & SPARKS, R. S. J. 1998 Experiments on bidisperse, constant-volume gravity currents: propagation and sediment deposition. *Sedimentology* **45**, 833–843.

HODSON, J. M. & ALEXANDER, J. 2010 The effects of grain-density variation on turbidity currents and some implications for the deposition of carbonate turbidites. *J. Sedim. Res.* **80**, 515–528.

HUANG, H., IMRAN, J. & PIRMEZ, C. 2007 Numerical modelling of poorly sorted depositional turbidity currents. *J. Geophys. Res.* **112**, doi:10.1029/2006JC003778.

KNELLER, B. & BUCKEE, C. 2000 The structure and fluid mechanics of turbidity currents: a review of some recent studies and their geological implication. *Sedimentology* **47** (Suppl. 1), 62–94.

MCCAFFREY, W. D., CHOUX, C. M., BAAS, J. H. & HAUGHTON, P. D. W. 2003 Spatio-temporal evolution of velocity structure, concentration and grain-size stratification within experimental particulate gravity currents. *Mar. Petrol. Geol.* **20**, 851–860.

MARTIN, D. & NOKES, R. 1988 A fluid-dynamical study of crystal settling in convecting magmas. *Nature* **332**, 534–536.

MARTIN, D. & NOKES, R. 1989 A fluid-dynamical study of crystal settling in convecting magmas. *J. Petrol.* **30**, 1471–1500.

MEIBURG, E. & KNELLER, B. 2010 Turbidity currents and their deposits. *Annu. Rev. Fluid Mech.* **42**, 135–156.

MONAGHAN, J. J., MÉRIAUX, C. A., HUPPERT, H. E. & MONAGHAN, J. M. 2009*a* High Reynolds number gravity currents along V-shaped valleys. *Eur. J. Mech. (*B/*Fluids* **28**, 651–659.

MONAGHAN, J. J., MÉRIAUX, C. A., HUPPERT, H. E. & MANSOUR, J. 2009*b* Particulate gravity currents along V-shaped valleys. *J. Fluid Mech.* **631**, 419–440.

SALAHELDINA, T. M., IMRANA, J., CHAUDHRYA, M. H. & REED, C. 2000 Role of fine-grained sediment in turbidity current flow dynamics and resulting deposits. *Mar. Geol.* **171**, 21–38.

SPARKS, R. S. J. 1976 Grain size variations in ignimbrites and implications for the transport of pyroclastic flows. *Sedimentology* **23**, 147–188.

WANG, L. P. & MAXEY, M. R. 1993 Settling velocity and concentration distribution of heavy particles in homogeneous isotropic turbulence. *J. Fluid Mech.* **256**, 27–68.